

Available online at www.sciencedirect.com

ScienceDirect

Acta Materialia 73 (2014) 326–336

www.elsevier.com/locate/actamat

Revisiting the CuPt₃ prototype and the L₁₃ structure

Chumani Mshumi^a, Candace I. Lang^{a,1}, Lauren R. Richey^b, K.C. Erb^b,
 Conrad W. Rosenbrock^b, Lance J. Nelson^b, Richard R. Vanfleet^b, Harold T. Stokes^b,
 Branton J. Campbell^b, Gus L.W. Hart^{b,*}

^a Centre for Materials Engineering, Department of Mechanical Engineering, University of Cape Town, South Africa

^b Department of Physics and Astronomy, Brigham Young University, Provo, UT 84602, USA

Received 20 December 2013; received in revised form 9 March 2014; accepted 14 March 2014

Available online 9 May 2014

Abstract

Experimentally and computationally, the structure of Pt–Cu at 1:3 stoichiometry has a convoluted history. The L₁₃ structure has been predicted to occur in binary alloy systems, but has not been linked to experimental observations. Using a combination of electron diffraction, synchrotron X-ray powder diffraction, and Monte Carlo simulations, we demonstrate that it is present in the Cu–Pt system at 1:3 stoichiometry. We also find that the 4-atom, fcc superstructure L₁₃ is equivalent to the large 32-atom orthorhombic superstructure reported in older literature, resolving much of the confusion surrounding this composition. Quantitative Rietveld analysis of the X-ray data and qualitative trends in the electron-diffraction patterns reveal that the secondary $X_1^+(a, 0, 0)$ order parameter of the L₁₃ phase is unexpectedly weak relative to the primary $L_1^+(a, a, 0, 0)$ order parameter, resulting in a partially-ordered L₁₃ ordering, which we conclude to be the result of kinetic limitations. Monte Carlo simulations confirm the formation of a large cubic superstructure at high temperatures, and its eventual transformation to the L₁₃ structure at lower temperature, but also provide evidence of other transitional orderings.

© 2014 Acta Materialia Inc. Published by Elsevier Ltd. All rights reserved.

Keywords: Diffraction; Ordering; Alloys; Platinum; Catalysis

1. Introduction

The structure of Cu–Pt at 1:3 stoichiometry was first reported by Schneider and Esch in 1944 [1] as an orthorhombic ordering that can be visualized as a 32-atom fcc supercell (see Fig. 1(a)). This result was followed by conflicting reports over the next three decades [2–7]. In 1974, Miida and Watanabe resolved the contradictions by dem-

onstrating that the 32-atom orthorhombic ordering is indeed the stable structure in CuPt₃ at room temperatures, but that rhombohedral and cubic orderings also appear in the phase diagram at adjacent compositions and temperatures [8].

On the theoretical side, the story is also rather convoluted. Based on theoretical considerations, Khachatryan's formalism is consistent with a 4-atom orthorhombic unit cell as the prototype CuPt₃ structure [9] but he incorrectly cites the 32-atom cell of cubic symmetry proposed by Tang (see Ref. [2]), which can be condensed to an 8-atom primitive cell, and diagrams a tetragonal 32-atom cell that seems to be a hybrid of the orthorhombic and cubic structures; see also Fig. 1 panes (b) and (d). The Khachatryan

* Corresponding author.

E-mail addresses: candace.lang@gmail.com (C.I. Lang), gus.hart@byu.edu (G.L.W. Hart).

¹ Current address: Department of Engineering, Macquarie University, Sydney, Australia.

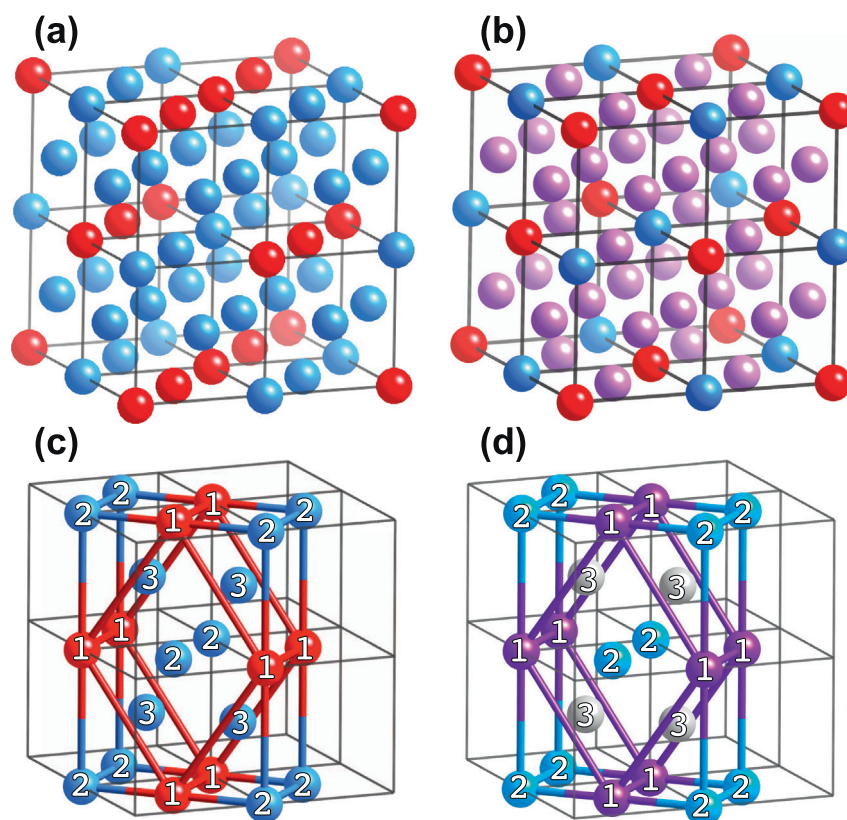


Fig. 1. (a) The originally proposed [1] orthorhombic structure for CuPt_3 , where Pt atoms are shown in blue and Cu atoms in red. This 32-atom cell is not primitive (or even conventional) but clearly shows the ordering motif and the underlying fcc parent lattice. (b) A CuPt_3 ordering model proposed by Tang [2], wherein both the $2 \times 2 \times 2$ supercell and the parent cell have face-centered cubic symmetry. Despite the 3:1 stoichiometry, one of the sites (indicated by purple atoms) is disordered, i.e. randomly occupied by both Pt and Cu atoms. (c) The conventional C-centered orthorhombic unit cell of L1_3 first discussed by Khachaturyan and proposed as the structure of CuPt_3 , which is crystallographically equivalent to that of (a). The smaller 4-atom primitive cell is indicated by red lines. The numerals 1, 2, and 3 indicate distinct Wyckoff positions and are discussed later. (d) The structure of L1_3 as determined from present experiments. Gray atoms indicate a disordered site, while purple atoms indicate a partially-ordered site that is Cu-rich but not pure Cu.

orthorhombic cell² is now referred to by the *Strukturbericht* symbol L1_3 .³

² Although the 4-atom cell that Khachaturyan introduced in Ref. [9] is orthorhombic, he referred to it as a tetragonal cell. Subsequent references to this special Lifshitz structure in the theoretical literature recognize it as orthorhombic.

³ This arbitrary Strukturbericht-like designation is motivated by other official designations. Strukturbericht designations for pure elements start with A; the face centered cubic (fcc) structure is A1. One-to-one structure designations start with B; the NaCl structure is designated B1, the 1 coming from A1, indicating fcc. Alloy structures are indicated by a beginning L and fcc-based alloys L1, again the 1 indicating fcc. A second, subscripted number in the Strukturbericht symbol, L1_x , indicates the order of discovery or assignment. For example, the designation for CuAu is L1_0 , indicating that CuAu was the first fcc-based alloy to be given a symbol. Next, was the designation for equiatomic PtCu as L1_1 , and so forth. The designation of the 4-atom, orthorhombic structure shown in Fig. 1(d) as L1_3 follows this convention. However, adding to the potential confusion, the Strukturbericht symbol L1_3 was already used in 1931 [10] for another structure (an 8-atom cell of 1:1 stoichiometry but not that referred to as D4 in the modern community). Apparently, the previous use of the symbol was forgotten by the modern community. It is possible that there are instances, besides [10] in the literature (past or current), where L1_3 designation is used for the previous structure but the authors are not aware of any.

Although, it was never recognized experimentally, L1_3 has long been employed as a hypothetical structure in the alloy community, due both to the work of Khachaturyan and the seminal work of Kanamori and Kakehashi where it is derived as a possible alloy structure on purely theoretical grounds [11]. No work in the experimental literature has discussed the primitive unit cell of the (original, 1944) 32-atom orthorhombic supercell, and no work in the computational/theoretical literature has recognized that the L1_3 structure is related to the experimental structure of Schneider [12]. Here, we make the simple observation that the ordering conveyed by Schneider's original orthorhombic 32-atom supercell is in fact equivalent to the 4-atom L1_3 structure (shown in Fig. 1(c)), which is also orthorhombic.

The L1_3 structure emerges naturally from the concentration wave formalism [9,13] as a Lifshitz structure associated with the k -points $(\frac{1}{2}, \frac{1}{2}, \frac{1}{2})$ and $(1, 0, 0)$. It also emerged independently from the cluster expansion community, where ordered superstructures of a disordered fcc parent were enumerated for ground state searches using Ising models of alloys [11,14–17]; but it was not considered to be especially interesting until it was predicted to be a stable

configuration in the Ag–Pd system in 2001 (where it was called $L1_1^+$ because of its relationship to the $L1_1$ structure [18]). Curtarolo predicted it as a ground state structure in Pd–Pt and Cd–Pt [19]; and it was discussed as a likely “missing structure” in the enumeration-related work of Hart [20].

The interest in $CuPt_3$ is not merely academic—it has practical import. Much research has been done on the catalytic properties of platinum and platinum-based alloys because of their widespread use in the chemical and petroleum industries. Additionally, the use of platinum-alloys in the jewelry industry accounts for a sizeable fraction of the worldwide consumption of platinum alloys, about 30% over the last decade [21]. In both cases, knowing the composition and structure of stable compounds is useful for materials improvement and design. It is surprising then that so little is known about the structural and mechanical properties of these alloys, knowledge that could be used to improve Pt-based jewelry alloys [22] and catalysts.

The most common alloying element in platinum jewelry is Cu in relatively low concentration. Although Pt–Cu has been extensively used by jewelers for more than 100 years, the influence of the cubic 7:1 phase [1], which can dramatically harden the alloy when it is present even in small volume fractions [22], was only recently confirmed [23]. It is important to remember that even well-known alloys harbor surprises, and that novel alloy orderings can have significant impact on practical material performance.

The $L1_3$ structure was very recently predicted to be the stable phase of Cu–Pt at the 1:3 stoichiometry in Ref. [24]. It was this prediction that led to the present re-examination of the room-temperature structure of $CuPt_3$, where electron diffraction and X-ray powder diffraction measurements unambiguously identify the supercell and quantify the Pt and Cu occupancy fractions at each site, which turn out to be roughly consistent with $L1_3$. This reexamination clarifies the apparent discrepancies in previous work, connects first-principles predictions and experimental evidence in the Cu–Pt system, and provides a pathway towards the engineering of Cu–Pt alloys with superior properties.

2. Methods

Buttons of Cu 75 at.% Pt were prepared by arc-melting on a copper hearth. The thickness of a cast button was first reduced by 50% in a rolling mill, after which the alloy was homogenised in argon at 1000 °C for 24 h, terminated by quenching. The buttons were then reduced a further 90% by rolling. We checked composition (1) by carrying out SEM–EDS on the as-cast button; (2) by carrying out TEM–EDS on the TEM foils which were used for imaging and diffraction. In each case, composition was evaluated at a number of points and averaged; the average was within 1 at.% of 25 at.% Cu, 75 at.% Pt.

Disks for transmission electron microscopy (TEM) were cut from this cold rolled sheet and subjected to heat treatments between 100 °C and 800 °C in an argon atmosphere,

terminated by quenching. Grinding and dimpling were followed by final thinning to perforation using a Gatan Precision Ion Polishing System.

The $CuPt_3$ sample used to collect synchrotron powder X-ray diffraction (PXD) data was prepared by 90% cold working and subsequent annealing at 350 °C for 2 months. Quantitative Rietveld analysis was performed using the TOPAS Academic (TA) software package.

Electron microscopy images and electron diffraction patterns were collected using a Tecnai F20 TEM, operating at 200 kV, by combining selected-area electron diffraction (SAED) and dark-field (DF) imaging. In situ heating was performed using a Gatan heating specimen stage in the TEM. For comparison with experimental results, the candidate structures and associated electron diffraction patterns were generated using CrystalMaker and SingleCrystalTM software respectively.

Laboratory PXD data from a rolled foil of 1 mm thickness proved inadequate for Rietveld analysis due to the highly-oriented rolling texture and due to the weakness of the superlattice reflections. The samples were too small and expensive to grind into powders in amounts sufficient for flat-plate reflection-geometry experiments, but we did attempt a transmission-geometry experiment with a finely-ground powder that was lightly distributed over the surface of a Kapton capillary tube (the $CuPt_3$ absorption length is approximately 3 μm at an X-ray wavelength of 1.54 Å); because the sample density was very low, the relative scattering contribution from the Kapton introduced far too much background and noise to allow the investigation of weak superlattice peaks.

To overcome the challenges presented by small samples of strongly-absorbing and highly-oriented materials, we designed and built a double-axis sample spinner (DASS) (see Fig. 2(a)) in order to orientationally average a small polycrystal in transmission mode, and also utilized high-energy (30 keV, $\lambda = 0.41346$ Å) synchrotron X-rays at beamline 11BM at the Advanced Photon Source at Argonne National Laboratory. Because the absorption length at this energy is 20 μm , a small button sample was polished down into a foil of 20 μm thickness and trimmed into a 2.5 mm \times 200 μm rectangle. In order to render the X-ray absorption as isotropic as possible, the rectangular foil was then roughly shaped into a half-cylinder with its axis parallel to the 2.5 mm dimension, and mounted on the tip of a steel needle (see Fig. 2(b)). The omega axis of the DASS was oriented perpendicular to the X-ray beam and parallel to the lab floor and rotated at a speed of 1 Hz, while the phi-axis, which is affixed to the moving omega stage, was inclined 54.74 ° relative to the omega axis and rotated at a speed of 10 Hz. The 2θ multi-detector bank was scanned in 0.005 ° increments while collecting data for 4 s per step. The time per point was intentionally set to an integer multiple of the DASS omega-axis period; incommensurability in this ratio results in undesirable cyclic background variations due to incomplete orientational averaging at each point. Because the detector bank had

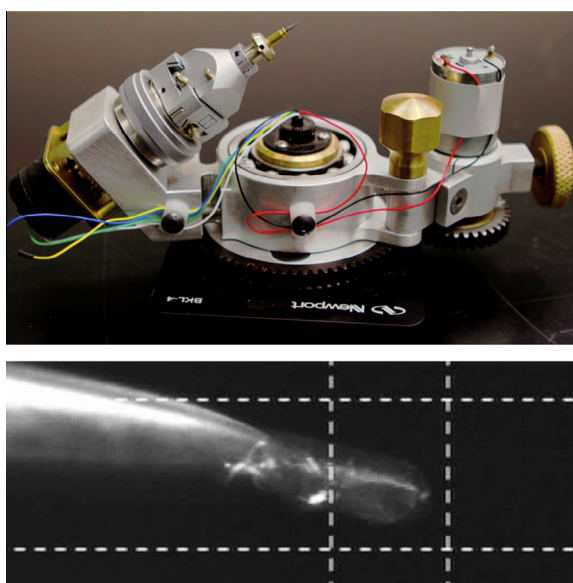


Fig. 2. (a) Gandolfi-type double-axis sample spinner for generating powder diffraction patterns from small polycrystals. The central omega axis (left) and inclined phi axis (right) are 54.74° apart for optimal orientational averaging and have independent motors that also act as counterweights. (b) Platinum alloy sample (mostly inside the center box) mounted to a steel needle tip (left side) at beamline 11BM. The $300\ \mu\text{m}$ X-ray beam is smaller than the region marked by the dashed lines. The sample spins around two axes while maintaining a fixed point at the center of the beam.

12 detectors spaced 2° apart, a 2° scan covered 24° , and two such scans provided coverage out to 48° . Each scan was collected 6 times and averaged, requiring about 6 h of collection time.

We used the UNCLE [25] software package to perform a classical, thermodynamic Monte Carlo simulation on a supercell that repeated the primitive unit cell 32 times in each direction. The simulation used 9×10^5 flips per averaging step, with each step terminating after energy convergence within 0.5 meV. Order parameters for the supercell at each temperature step were calculated using the mean of the charge occupancies (based on atomic number) at each site in a given crystallographic direction.

3. Results and discussion

3.1. Transmission electron microscopy

The electron diffraction patterns from initially cold worked Cu 75 at.% Pt in Fig. 3(a), as observed along the [100], [110], [112] and [103] zone axes, show the fundamental reflections expected from a disordered fcc alloy. After heat treatment at 350°C , additional reflections were observed (see Fig. 3(b)) halfway (1) along the $\{200\}$ and $\{220\}$ type directions in the [100] zone axis diffraction pattern, (2) along $\{200\}$, $\{111\}$ and $\{220\}$ in the $[110]_{\text{fcc}}$ pattern, (3) along $\{220\}$, $\{111\}$ and $\{131\}$ in the $[112]_{\text{fcc}}$ pattern, and (4) along $\{131\}$ and $\{200\}$ in the $[103]_{\text{fcc}}$ pattern. These reflections were observed following each heat

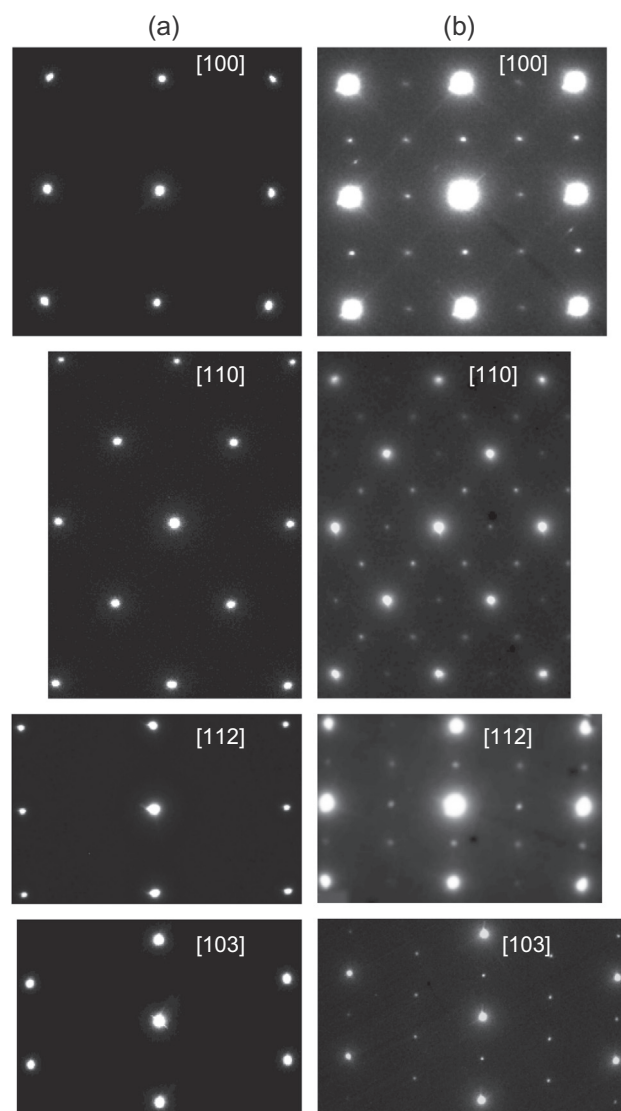


Fig. 3. Electron diffraction patterns from Cu 75 at.% Pt (a) initially cold worked; (b) after heat treatment at 350°C for 3 h; showing $[100]_{\text{fcc}}$, $[110]_{\text{fcc}}$, $[112]_{\text{fcc}}$, and $[103]_{\text{fcc}}$ zone axes. The heat treated specimen shows clear signs of ordering.

treatment between 200°C and 400°C , indicating that ordering had taken place. Note that the $\frac{1}{2}\{220\}$ and $\frac{1}{2}\{131\}$ reflections are related by translations of the parent-fcc reciprocal lattice to the $\frac{1}{2}\{200\}$ and $\frac{1}{2}\{111\}$ reflections in the first Brillouin zone. In fact, all of the observed superlattice reflections are related to either $\frac{1}{2}\{200\}$ or $\frac{1}{2}\{111\}$ by translations of the parent-fcc reciprocal lattice. Thus, it is not possible for the intensities at these points to arise from the double-diffraction of two parent-lattice reflections.

The $L1_3$ structure has several inequivalent viewing directions or variants that contain the same fundamental reflections but different superlattice reflections. Fig. 4 shows three $L1_3$ variants with the same $[100]_{\text{fcc}}$ zone axis. We find that the electron diffraction patterns shown in Fig. 3(b) are consistent with those expected from the $L1_3$ structure based on simulations. However, we also find that they are

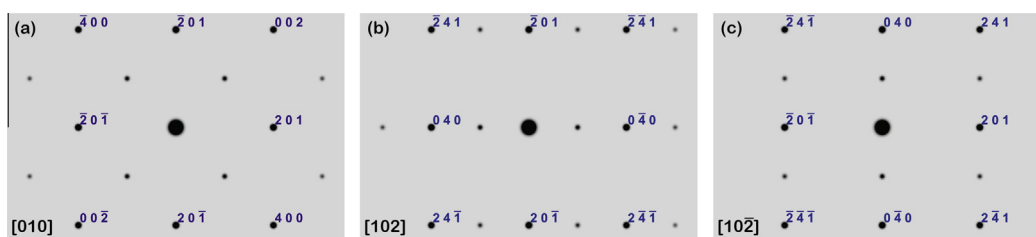


Fig. 4. Simulated electron diffraction patterns for three variant views of the $[100]_{\text{fcc}}$ zone axis diffraction pattern of the $L1_3$ structure of CuPt_3 . Only the fundamental reflections of the fcc parent structure are labeled, but using the setting of the ordered structure.

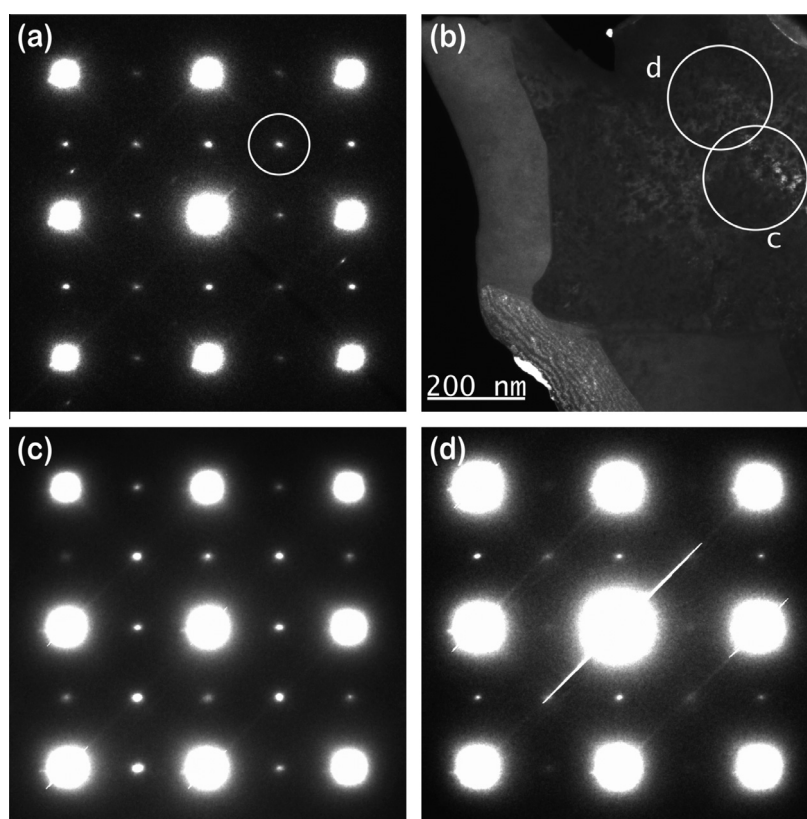


Fig. 5. Dark field images and selected area diffraction at different locations of the dark field image from CuPt_3 after heat treatment for 3 h at 350 °C: (a) shows a $[100]_{\text{fcc}}$ zone axis electron diffraction pattern from the whole grain; (b) is the dark field image made using the circled reflection in (a), with circled areas showing the regions from which selected area diffraction patterns (c) and (d) were acquired.

consistent with the 32-atom orthorhombic CuPt_3 structure of Schneider and Esch [1]. On closer inspection of Fig. 1(a and c), we discovered that the two orderings are crystallographically equivalent, a fact that does not appear to have been reported or discussed in previous literature. Thus, any subsequent mention of the *orthorhombic* ordering will implicitly refer to $L1_3$.

Each simulated pattern in Fig. 4 corresponds to the same experimental $[100]_{\text{fcc}}$ zone-axis pattern from Fig. 3(b), but lacks some of the experimentally-observed superlattice reflections. This is because the compositional ordering has a larger unit cell than the fcc parent structure, and therefore has distinct orientational variants. Each simulated pattern simulates only one of these variants. Because there is no orientation preference for nucleation of the $L1_3$

structure in the disordered alloy, the variant that appears within a given nucleating grain will be essentially random. Thus, any large-area diffraction pattern, such as those seen in Fig. 3(b), will sample all possible variants and will simultaneously exhibit all of their superlattice reflections. One critical feature of the work by Miida and Watanabe [8] was creating large enough ordered grains that distinctions between the variants could be observed. The presence of variants makes it possible to distinguish $L1_3$ from the $2 \times 2 \times 2$ cubic supercell, for which the $[100]_{\text{fcc}}$ zone axis diffraction pattern simultaneously contains the superlattice reflections from all three of the variants of Fig. 4.

Because the patterns in Fig. 3(b) are the result of averaging over multiple orientational variants of the ordered $L1_3$ structure, we collected dark-field images with a single

$\frac{1}{2}\{220\}$ type superlattice reflection within the $[100]_{\text{fcc}}$ pattern (Fig. 5(a)) to separate the distinct variants that give rise to $\frac{1}{2}\{200\}$ and $\frac{1}{2}\{220\}$ type superlattice reflections. The expected diffraction patterns of these variants are simulated in Fig. 4. Fig. 5(a) shows the diffraction from a large $[100]_{\text{fcc}}$ grain with the $\frac{1}{2}(220)$ used for the dark-field image circled with Fig. 5(b) showing the dark-field image with the central region being the $[100]_{\text{fcc}}$ grain. Sharp boundaries between intensities delineate different fcc grains and the mottled appearance within the $[100]_{\text{fcc}}$ grain is fluctuations of the $\frac{1}{2}\{220\}$ intensities. The two circles in Fig. 5(b) show the placement of a small SA aperture and indicate the regions from which diffraction patterns in 5(c) and 5(d) are taken. Because the ordered domains were roughly 10 nm in diameter, the size limitations of the microscope SA aperture made it difficult to fully isolate a single reflection type. However, regions c and d show a different mix of intensity in the additional superlattice reflections. Region c was chosen to contain both the brightest and darkest regions of the dark-field image and shows approximately equal intensities in the possible superlattice peaks while region d, which was chosen for its intermediate intensity, shows a strong set of $\frac{1}{2}\{200\}$ peaks above and below the central peak and a much weaker set of $\frac{1}{2}\{200\}$ peaks to the left and right of the central peak; the $\frac{1}{2}\{220\}$ peaks are also weak. This mix of intensities demonstrates that the variants required of the $L1_3$ structure are indeed present in our sample.

Following a heat treatment at or above roughly 400 °C, the pattern of superlattice reflections changes to that indicated in Fig. 6, where the $\frac{1}{2}\{200\}$ and related reflections are unexpectedly weak relative to the $\frac{1}{2}\{111\}$ and related

reflections. In the 350 °C-annealed samples of Fig. 3, however, these two types of reflections have more similar intensities.

In Figs. 3, 5 and 6, some strong Bragg reflections exhibit sharp streaks along $\{110\}$ directions. In most cases, (e.g., Fig. 5(d)), this is clearly a CCD-saturation artifact. Some of the weaker streaks are due to sweeping the diffraction pattern onto the CCD detector during a relatively short exposure. Because of the intense peaks in the diffraction pattern and the short exposure times, the sweep across the CCD leaves artifacts that can be seen in this case. We also note the presence of an unaccounted pair of reflections in the $[100]$ panels of Fig. 3(b) and 5(a), which appear to be $\{200\}$ reflections from a second grain.

3.2. X-ray diffraction

The synchrotron PXD data from samples annealed for two months at 350° were of exceptionally high quality and permitted the observation of many superlattice peaks, all of which could be indexed using the supercell associated with the $L1_3$ ordered structure (Fig. 1(c)): a C -centered conventional cell with basis vectors $(1, 0, 1)$, $(0, 2, 0)$, $(-\frac{1}{2}, 0, \frac{1}{2})$, and origin $(0, 0, 0)$ relative to the conventional basis vectors of the fcc parent. In fact, the $L1_3$ ordering is the only binary decoration of an fcc lattice consistent with this supercell. Thus, we used the $L1_3$ model as a starting point for quantitative Rietveld analysis. The final fit is shown in Fig. 7.

Because the background was somewhat structured, we fit it with a combination of a $1/x$ term for air scattering, a Chebychev polynomial and several extremely-broad

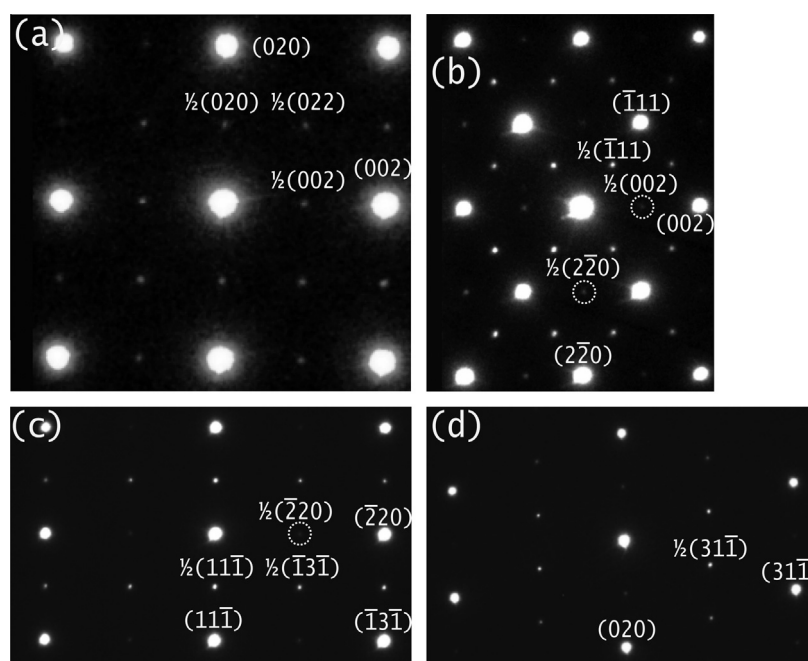


Fig. 6. Electron diffraction patterns from CuPt_3 after heat treatment for 3 h at 600 °C, showing (a) $[100]_{\text{fcc}}$, (b) $[110]_{\text{fcc}}$, (c) $[112]_{\text{fcc}}$, and (d) $[103]_{\text{fcc}}$ zone axes.

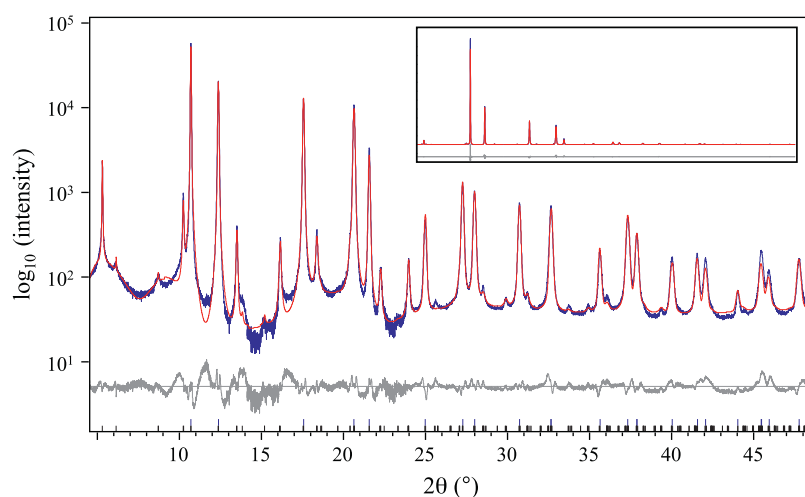


Fig. 7. Rietveld fit of a partially-ordered $L1_3$ model against synchrotron X-ray powder diffraction data ($\lambda = 0.4135 \text{ \AA}$) from CuPt_3 after heat treatment for 2 months at $350 \text{ }^\circ\text{C}$. Blue, red, and gray curves indicate the experimental data, the model calculation, and the difference, respectively. The short vertical black lines at the bottom indicate supercell peak positions, while the longer vertical blue rods indicate parent fcc peak positions. Intensities are presented on a log scale because all but a few of the superlattice reflections are otherwise too weak to see. Apparently large discrepancies on the weaker peaks are actually very small. The inset contains a view of the same fit on a linear vertical scale. (For interpretation of the references to colour in this figure legend, the reader is referred to the web version of this article.)

low-amplitude peaks. The peak shape was entirely strain dominated with widths that adhered to a distinct $\text{FWHM} = s \tan(\theta)$ trend. Furthermore, the superlattice peaks were distinctly broader than the fcc parent peaks, and were thus fitted with different shapes. The parent peaks exhibited a convolution of Lorentzian ($s = 0.442(2)^\circ$) and Gaussian ($s = 0.185(1)^\circ$) contributions, while the superlattice peaks were fitted with a purely Lorentzian ($s = 0.83(2)^\circ$) shape.

Despite an obviously correct supercell and a reasonably well-matched peak shape, the intensities were not well matched by a simple $L1_3$ ordering. The $L1_3$ structure has $Cmnm$ space-group symmetry and three distinct crystallographic sites (see Fig. 1(c)): #1 the two atoms at the cell corner and the center of the c -face, #2 the two atoms at the middle of the a and b cell edges, and #3 the four atoms within the interior of the supercell. Allowing these three site occupancies to vary, under the constraints that the total Pt + Cu occupancy at each site remains equal to 1 and the overall stoichiometry remains at Cu:Pt = 1:3, proved to be important; it lowered the R_{wp} residual factor from 55.4% to 28.5%. The result was a complete Pt order at site #2, but partial or complete disorder at the other two sites⁴.

Switching from isotropic (u_{iso}) to anisotropic (u_{ij}) thermal parameters further improved the fit, though the resulting anisotropy was so strong as to suggest the presence of site disorder. For this reason, we allowed each atom to fragment into a set of symmetry-related partial-occupancy pieces surrounding its ideal high-symmetry position. Com-

bined, with the anisotropic thermal parameters, this sophistication visibly improved the fit. Note that the site disorder only tended to displace atoms in the x and y direction of the supercell, leading us to fix the z -axis displacements to zero. Furthermore, strong correlations between the off-site displacements and the anisotropic thermal parameters required us to fix the u_{22} and u_{33} parameters of each site. Not only were the microscopic parameters of the Pt and Cu atoms sharing a common site tied together, but the same Δx , Δy , and u_{11} were shared by all three sites (u_{12} only applies to site #3). It seems reasonable to conclude that the compositional disorder on sites #1 and #3, coupled with the different relative atomic radii of Pt and Cu, results in local size-effect displacements that are manifested as displacive disorder and anisotropic thermal parameters. Including these effects lowered R_{wp} to 17.7%.

The peak-height discrepancies that remained showed a clearly sinusoidal trend that completed more than one full period across the diffraction pattern, and were not resolvable using any combination of parameters available to the atoms of the supercell. Speculating that this oscillation is further evidence of large size-effect displacements that cannot be accommodated by a simple atomistic average structure, we elected to accommodate this trend by multiplying all peak intensities by an empirical sinusoidal envelope of the form $1 + A \cos^2(B\theta - C)$, where $A = 0.62$, $B = 0.36$, and $C = 6.5$ were fitting parameters. While such a term is unorthodox, it produced a clean overall fit with $R_{\text{wp}} = 10.9\%$ that improved our confidence in the other structural parameters.

The values of all other refined structural parameters described above appear in Table I, where statistical error estimates appear in parentheses. The compositional disorder on sites #1 and #3 clearly leads to substantial size-effect-induced displacive disorder. It is interesting that

⁴ Because the $Cmnm$ symmetry provides no displacive degrees of freedom to the $L1_3$ structure, we also tried lowering the symmetry to $P1$ within the primitive supercell, and used simulated annealing to optimize small displacements of 8 atoms in the supercell; but this did not reliably improve the fit. So we returned to the $Cmnm$ symmetry in all subsequent attempts.

Table I

Tabulated results from the Rietveld refinement of the orthorhombic $L1_3$ model against synchrotron PXD data from CuPt_3 , where $a = 7.6763(1)$, $b = 5.4405(2)$, $c = 2.7204(1)$, $\Delta y = 0.0428(1)$, $\Delta z = 0.0394(3)$, $u_{11} = 0.0131(2)$, $u_{12} = 0.0108(5)$, and $R_{\text{wp}} = 10.9\%$.

Atom	x	y	z	occ	u_{11}	u_{22}	u_{33}	u_{12}	u_{13}	u_{23}
Pt1	0	$0 + \Delta y$	$0 + \Delta z$	0.497(4)	u_{11}	0^*	0^*	0	0	0
Cu1	0	$0 + \Delta y$	$0 + \Delta z$	0.503(4)	u_{11}	0^*	0^*	0	0	0
Pt2	0	$1/2 + \Delta y$	$0 + \Delta z$	1.073(4)	u_{11}	0^*	0^*	0	0	0
Cu2	0	$1/2 + \Delta y$	$0 + \Delta z$	0.073(4)	u_{11}	0^*	0^*	0	0	0
Pt3	$\frac{1}{4}$	$\frac{1}{4} + \Delta y$	$1/2 + \Delta z$	0.712(3)	u_{11}	0^*	0^*	u_{12}	0	0
Cu3	$\frac{1}{4}$	$\frac{1}{4} + \Delta y$	$1/2 + \Delta z$	0.288(3)	u_{11}	0^*	0^*	u_{12}	0	0

the atomic displacements have magnitudes on the order of 0.1 to 0.25 Å, which are comparable to the difference between the nearest-neighbor distances in fcc Pt (2.775 Å) and Cu (2.556 Å) at room temperature.

3.3. Interpretation

Assuming that the total occupancy (Pt + Cu) of each symmetry-unique site is constrained to equal 1, and that the overall stoichiometry is fixed during the composition-ordering process, a complete description of the $L1_3$ ordering (space group $Cmmm$) has two independent variables. Using group representational analysis, we associated these variables with irreducible matrix representations (IRs) of the parent $Fm\bar{3}m$ space group. Using the ISODISTORT software package [26], we find that the first variable is an $(a, a, 0, 0)$ order parameter of the L_1^+ IR at the reciprocal-space $L(\frac{1}{2}, \frac{1}{2}, \frac{1}{2})$ point, while the second variable is an $(a, 0, 0)$ order parameter of the X_1^+ IR at the reciprocal-space $X(1, 0, 0)$ point. Of the two contributing order parameters, $L_1^+(a, a, 0, 0)$ is primary in the sense that its action alone is sufficient to produce the observed supercell and space-group symmetry. $X_1^+(a, 0, 0)$ is secondary because it is consistent with the symmetry of the primary order parameter, but cannot achieve such a low symmetry by itself. $X_1^+(a, 0, 0)$, when acting alone, would result in the $L1_0$ structure, which is the most common ordering among all 1:1 binary alloys. Each superlattice reflection that results from the ordering differs from one of these two points by a parent lattice vector, and is therefore associated with the corresponding order parameter. The relative intensities of the L and X -type superlattice reflections then gauge the relative contributions of their respective order parameters. Together, these two order parameters provide a natural symmetry-based description of deviations from the fcc structure.

Static concentration waves at the L and X points of $Fm\bar{3}m$ have been used previously to describe ordering in copper platinum alloys [9,27,28], though they were not labeled in this way. A proper group-representational description of the concentration waves is completely consistent with their observations, but reveals fundamental problems with their terminology, wherein they incorrectly associated all L -point waves with the label $L1_1$ and all X -point waves with the label $L1_2$.

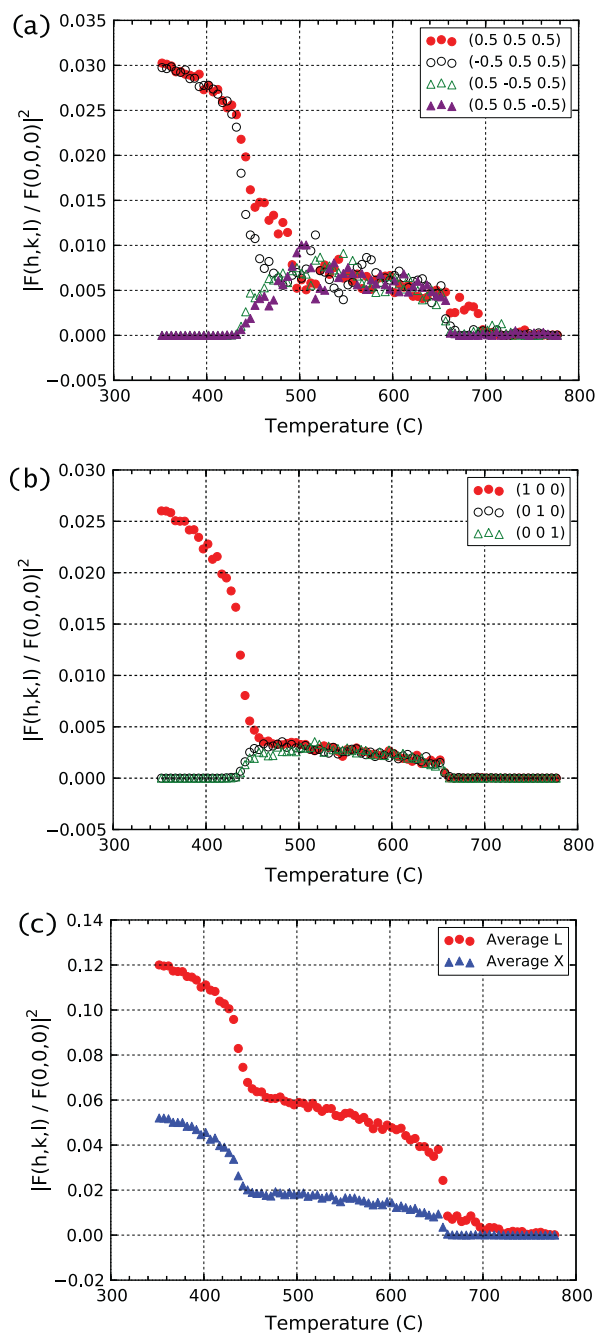


Fig. 8. Simulated kinematic superlattice intensities associated with the X and L -points derived from Monte-Carlo simulations: (a) the four L -point reflections, (b) the three X -point reflections, (c) powder averages of the X and L -point intensities taking reflection multiplicity into account.

The star of the L point includes four vectors: $(\frac{1}{2}, \frac{1}{2}, \frac{1}{2})$, $(\frac{1}{2}, -\frac{1}{2}, -\frac{1}{2})$, $(-\frac{1}{2}, \frac{1}{2}, -\frac{1}{2})$, and $(-\frac{1}{2}, -\frac{1}{2}, \frac{1}{2})$; and the star of the X point includes three vectors: $(1, 0, 0)$, $(0, 1, 0)$, and $(0, 0, 1)$. $L_1^+(a, 0, 0, 0)$ is primary for the $L1_1$ ordering stable at 50% Pt, and uses only one L -point vector. $L_1^+(a, a, 0, 0)$ is primary for the $L1_3$ ordering near 75% Pt, and uses two L -point vectors. $L_1^+(a, a, a, a)$ is primary for the large-cubic ordering just above 75% Pt, and uses all four L -point vectors. $L_1^+(a, b, b, b)$ is primary for the large-rhombohedral ordering just below 75% Pt, and uses all four L -point vectors; it can be viewed as a superposition of $L1_1$ and the large-cubic ordering. $X_1^+(a, a, a)$ is primary for $L1_2$ order, which is reported to be stable at 25% Pt (Ref. [8]); it uses all three X -point vectors; it is secondary to both the large-cubic and large-rhombohedral orderings. $X_1^+(a, 0, 0)$, which uses only one X -point vector, is primary for $L1_0$ order but not observed at 50% Pt; it is also secondary for $L1_3$ ordering near 75% Pt. This more complete analysis reveals that the Cu–Pt phase diagram involves many different structure types, and cannot be summarized merely in terms of the labels $L1_1$ and $L1_2$, as was done previously [27,28].

The temperature-dependent Monte Carlo simulations of Fig. 8 indicate at least two phase transitions upon cooling from the high-temperature disordered state, though we are not able to infer accurate phase-transition temperatures from this output. The first panel tracks the relative intensities of the four $\frac{1}{2}[111]$ reciprocal-space reflections in the kinematic approximation, which correspond to the four components of the $L_1^+(a, b, c, d)$ order parameter. The second panel tracks the relative intensities of the three $\frac{1}{2}[200]$ reflections, which correspond to the three components of the $X_1^+(a, b, c)$ order parameter. The third panel tracks the powder-average intensities associated with the L and X reflections. Upon cooling, near 660 °C, all four L components take on comparable values and all three X component values take on comparable values, indicating the formation of the large $2 \times 2 \times 2$ cubic supercell of Tang [2]. Then in the vicinity of 480 °C, two of the L components begin to rise towards a new maximum while the other two drop to zero, and one of the X components begins to rise towards a new maximum, while the other two drop to zero; this indicates a transition to the $L1_3$ structure.

This computational result is consistent with the basic features of the phase diagram of Miida and Watanabe [8]. However, a closer inspection of the simulation output reveals additional subtleties; one of the L components clearly activates at a high temperature than the other L or X components indicating the narrowly limited presence of an $L1_1$ transitional phase between 660 °C and 690 °C. Furthermore, between 480 °C and 520 °C, one of the L components is significantly larger than the other three (though the various components appear to take turns being the large one), indicating the presence of a transitional phase with the large-rhombohedral supercell. Finally, between 430 °C and 480 °C, the two large L components don't immediately acquire the same intensity, indicating a

further lowering of the point symmetry of the transitional phase to monoclinic. Our experimental mesh of temperatures was much too coarse for the detection of such subtle phase variations, though an attempt to observe them might be worthwhile.

The PXD Rietveld analysis is only sensitive to the average L and X -component intensities due to overlap of equivalent reflections. For the refinement of the disordered $L1_3$ phase, rather than refining each atomic occupancy independently, we refined the order parameters directly, which are related to the Cu occupancies as follows.

$$\begin{aligned} \text{occ}(\text{Cu1}) &= \frac{1}{4} + \frac{1}{2}S_L + \frac{1}{4}S_X \\ \text{occ}(\text{Cu2}) &= \frac{1}{4} - \frac{1}{2}S_L + \frac{1}{4}S_X \\ \text{occ}(\text{Cu3}) &= \frac{1}{4} - \frac{1}{4}S_X \end{aligned}$$

Here, S_L is a factor of $\sqrt{2}$ larger than the normalized $L_1^+(a, a, 0, 0)$ order parameter used by ISODISTORT, and S_X is $\sqrt{2}$ times larger than the normalized $X_1^+(a, 0, 0)$ order parameter used by ISODISTORT. The unnormalized parameters conveniently run from 0 in the case of complete disorder to 1 in the case of long-range order, and are similar to those used in the static concentration-wave theory of Khachaturyan [9], who used the symbol η rather than S . Because all of the atomic occupancies must lie between 0 and 1, we simply require that $S_L \leq \frac{1}{2} + \frac{1}{2}S_X$.

From the Rietveld analysis of the sample annealed for two months at 350°, the fitted values in Table I show that $S_L = 0.430$ has a large value, whereas $S_X = 0.051$ is quite small in comparison, resulting in a partially-ordered version of $L1_3$, as illustrated in Fig. 1(d). For fully ordered $L1_3$, we would instead have $S_L = S_X = 1$. The role of the $L_1^+(a, a, 0, 0)$ is to shift Cu from site #2 to site #1, which can only proceed alone until site #2 is completely empty of Cu. If $S_X = 0$ for CuPt_3 , the limiting value of S_L is $\frac{1}{2} + \frac{1}{2} \cdot 0 = 0.5$, which enriches site #1 to the level of 50% Cu without affecting the composition of site #3. $X_1^+(a, 0, 0)$ should complete the $L1_3$ structure by transferring the residual 25% Cu on site #3 to site #1; despite its failure to do so, the overall Cu fraction remains at $\frac{1}{8}(2 \cdot \frac{1}{2} + 2 \cdot 0 + 4 \cdot \frac{1}{4}) = \frac{1}{4}$, as expected, where site multiplicities have been taken into account. The fitted values of $S_X \approx 0$ and $S_L \approx 0.5$ indicate that $L_1^+(a, a, 0, 0)$ is contributing close to the maximum amount possible given the small value of $X_1^+(a, 0, 0)$.

Unexpectedly small values for the X -point order parameters were also evident in electron diffraction data from samples annealed at temperatures higher than 350 °C, including those in the range where the large-cubic ordering is expected, e.g. Fig. 6. The Monte Carlo simulations of Fig. 8 don't support a thermodynamically stable phase with such a small X/L intensity ratio, even in the transitional region between the $L1_3$ and large-cubic phases. The expected ratios are considerably less than one, but the observed intensity ratios are at least four times smaller

than expected. And even if such an ordering were stable, it would be very unusual for a secondary order parameter to become active at a substantially lower temperature than its primary; the opposite is normally true, as seen, for example, in the CuMnPt₆ system [28,29]. For this reason, we suspect that the small X/L order-parameter ratio and its associated compositional disorder are due to kinetic limitations. We find that the energy of the L1₃ structure is far more sensitive to $L_1^+(a, a, 0, 0)$ order parameter than it is to $X_1^+(a, 0, 0)$, which provides one possible explanation for the relative kinetic difficulty of forming the X order parameter. But we don't understand why such limitations would be more restrictive for the samples that were annealed at higher temperatures. It could also be that slight cold-working and polishing during sample preparation (in the case of the sample used for Rietveld analysis) disrupted the X order parameter.

4. Summary

The ordered CuPt₃ alloy was first proposed and presented as a 32-atom orthorhombic superstructure [1] based on X-ray diffraction data, but subsequent experimental identification of two other distinct phases at about this stoichiometry have confused the issue. Work by Miida [8], and also our cluster-expansion-based Monte Carlo simulations, have shown the 32-atom orthorhombic ordering is stable for room-temperature CuPt₃, but that these other phases are present in nearby regions of the phase diagram.

To date, no ordered alloy has been experimentally associated with the hypothetical L1₃ structure employed in the computational arena. It is of particular interest that, prior to the present work, the L1₃ structure has not been experimentally associated with the CuPt₃ alloy. Instead, the 32-atom orthorhombic structure is often referenced as the stable structure for this stoichiometry. We observe that the two structures have identical simulated diffraction patterns, and that the atomic arrangements are in fact crystallographically equivalent. The fact that years of work in the computational arena failed to make this connection strongly suggests that the primitive unit cells of other alloy systems should be reevaluated. Identifying these two structures as one and the same should help to clear up past confusion surrounding the Pt-rich side of the Cu–Pt phase diagram.

TEM images and electron diffraction patterns show that our cold-worked samples of CuPt₃ became compositionally ordered after annealing at relatively low temperatures. Bright and dark-field electron diffraction patterns from multiple orientational variants confirmed the primitive unit cell to be that of L1₃ at 350 °C. Monte Carlo simulations show that CuPt₃ first forms a large-cubic supercell upon cooling from the disordered state, and subsequently forms the L1₃ phase, in basic agreement with the phase diagram of Miida and Watanabe [8]. These simulations also indicate the stability of L1₁ and large-rhombohedral transitional phases within narrow temperature ranges.

An innovative data collection strategy yielded high-quality synchrotron powder-diffraction data from small poly-crystalline foil fragments that suffer from extreme preferred orientation. We are not aware of comparable experiments involving metallic alloys. Using a sample annealed at 350 °C for two months, X-ray Rietveld analysis confirmed that essentially 100% of the sample material had ordered, though the ordering itself was not incomplete due to an unexpectedly low value of the $X_1^+(a, 0, 0)$ over $L_1^+(a, a, 0, 0)$ ratio, which we judge to result from non-thermodynamic considerations.

Acknowledgments

Financial support for CM, RRV, and CIL from the National Research Foundation (South Africa) is gratefully acknowledged. GLWH, LRR, BJC, CWR, and KCE are grateful for support from the National Science Foundation, DMR-0908753. RRV is grateful for support from the National Science Foundation, DMR-0906385. Use of the Advanced Photon Source, an Office of Science User Facility operated for the U.S. Department of Energy (DOE) Office of Science by Argonne National Laboratory, was supported by the U.S. DOE under Contract No. DE-AC02-06CH11357. A discussion with Roman Chepulskii regarding the concentration wave formalism is appreciated. GLWH and CWR are grateful for use of the Fulton Supercomputer Lab at Brigham Young University.

References

- [1] Schneider A, Esch U. *Z Elektrochem* 1944;50.
- [2] Tang Y-C. *Acta Crystallogr* 1951;4:377. ISSN 0365-110X.
- [3] Wu N-C, Iwasaki H, Ogawa S. *Trans Jpn Inst Metals* 1973;14:309.
- [4] Hansen M, Anderko K. *Constitution of binary alloys. Metallurgy and metallurgical engineering series, vol. 1.* McGraw-Hill; 1965.
- [5] Hirone T, Adachi K. *Sci Rep RITU* 1955;A-7:282.
- [6] Nagasaki S, Hirone T, Kono H. *Phys Soc Jpn*; 1955 [unpublished].
- [7] Ogawa S, Iwasaki H, Terada A. *J Phys Soc Jpn* 1973;34:384.
- [8] Miida R, Watanabe D. *J Appl Crystall* 1974;7:50.
- [9] Khachatryan AG. *Progress Mater Sci* 1978;22:1. ISSN 0079-6425.
- [10] Ewald VPP, Hermann C. *Strukturbericht 1913–1928* (Akademische Verlagsgesellschaft M.B.H., 1931).
- [11] Kanamori J, Kakehashi Y. *J Phys* 1977;38:274.
- [12] Hart GLW. *Phys Rev B* 2009;80:014106.
- [13] Fontaine DD. *Cluster approach to order-disorder transformations in alloys, vol. 47.* New York: Academic Press; 1994.
- [14] Ferreira LG, Wei S-H, Zunger A. *Int J Supercomput Appl* 1991;5:34.
- [15] Hart GLW, Forcade RW. *Phys Rev B* 2008;77:224115.
- [16] Hart GLW, Forcade RW. *Phys Rev B* 2009;80:014120.
- [17] Hart GLW, Nelson LJ, Forcade RW. *Comp Mater Sci* 2012;59:101.
- [18] Müller S, Zunger A. *Phys Rev Lett* 2001;87:165502.
- [19] Curtarolo S, Morgan D, Ceder G. *Calphad* 2005;29:163.
- [20] Hart GLW. *Nat Mater* 2007;6:941.
- [21] Jollie D. *Tech Rep, Johnson Matthey*; 2009.
- [22] Carelse M, Lang CI. *Scripta Mater* 2006;54:1311. ISSN 1359-6462.
- [23] Saha DK, Shishido T, Iwasaki H, Ohshima K. *J Phys Soc Jpn* 2003;72:1670.
- [24] Nelson LJ, Hart GLW, Curtarolo S. *Phys Rev B* 2012;85:054203.
- [25] Lerch D, Wieckhorst O, Hart GLW, Forcade RW, Müller S. *Model Simul Mater Sci Eng* 2009;17:055003.

- [26] Campbell BJ, Stokes HT, Tanner DE, Hatch DM. *J Appl Crystallogr* 2006;39:607.
- [27] Iwasaki H, Ohshima K. *J Phys Soc Jpn* 2005;74:2496.
- [28] Takahashi M, Das AK, Sembiring T, Iwasaki H, Ohshima K-I. *Physica B – Condensed Matter* 385:2006;130. In: 8th International conference (ICNS 2005), Sydney, Australia, November 27–December 02; 2005.
- [29] Takahashi M, Sembiring T, Yashima M, Shishido T, Ohshima K. *J Phys Soc Jpn* 2002;71:681. ISSN 0031-9015.